Enhancement of hydrogen storage performance in shell and tube metal hydride tank for fuel cell electric forklift

Hanbin Wang[a,b], Miao Du[c,d], Qi Wang[c,d], Zhipeng Li[a,b,*], Shumao Wang[c,d], Zhengming Gao[a,b,*], J.J. Derksen[e]

[a] Beijing Advanced Innovation Center for Soft Matter Science and Engineering, Beijing University of Chemical Technology, Beijing 100029, China

[b] State Key Laboratory of Chemical Resource Engineering, School of Chemical Engineering, Beijing University of Chemical Technology, Beijing 100029, China

[c] National Engineering Research Center of Nonferrous Metals Materials and Products for New Energy, GRINM Group Co., Ltd., Beijing, 100088, China

[d] GRIMAT Engineering Institute Co., Ltd., Beijing, 101407, China

[e] School of Engineering, University of Aberdeen, Aberdeen AB24 3UE, UK

*Corresponding authors. Tel.: +8610 64418267; fax: +8610 64449862. E-mail address: lizp@buct.edu.cn (Zhipeng Li), gaozm@buct.edu.cn (Zhengming Gao).

Abstract

Novel metal hydride (MH) hydrogen storage tanks for fuel cell electric forklifts have been presented in this paper. The tanks comprise a shell side equipped with 6 baffles and a tube side filled with 120 kg AB_5 alloy and 10 copper fins. The alloy manufactured by vacuum induction melting has good hydrogen storage performance, with high storage capacity of 1.6 wt% and low equilibrium pressure of 4 MPa at ambient temperature. Two types of copper fins, including disk fins and corrugated fins, and three kinds of baffles, including segmental baffles, diagonal baffles and hole baffles, were applied to enhance the heat transfer in metal hydride tanks. We used the finite element method to simulate the hydrogen refueling process in MH tanks. It was found that the optimized tank with corrugated fins only took 630 s to reach 1.5 wt% saturation level. The intensification on the tube side of tanks is an effective method to improve hydrogen storage performance. Moreover, the shell side flow field and hydrogen refueling time in MH tanks with different baffles were compared, and the simulated refueling time is in good agreement with the experimental data. The metal hydride tank with diagonal baffles shows the shortest hydrogen refueling time because of the highest velocity of cooling water. Finally, correlations regarding the effect

of cooling water flow rate on the refueling time in metal hydride tanks were proposed for future industrial design.

Keywords

Metal hydride tank; AB_5 alloy; Hydrogen storage; Tube side fins and shell side baffles;

Dimensionless correlations

Nomenclature

a_i	Polynomial coefficients of equilibrium pressure (MPa)
B	MH tank width (mm)
C	Hydrogen storage capacity of MH bed (-)
C_p	Specific heat capacity (J/kg/K)
D_{in}	Inner diameter of MH tube (mm)
D_{out}	Outer diameter of MH tube (mm)
d_{out}	Outer diameter of filter tube (mm)
H	MH tank height (mm)
H_f	Corrugated fin height (mm)
H_c	Metal hydride compact thickness (mm)
H_t	MH tube spacing (mm)
L	MH tank length (mm)
L_f	Corrugated fin length (mm)
L_b	Baffle spacing (mm)
M	Molecular mass (kg/mol)
P	Hydrogen pressure (MPa)
P_{eq}	Absorption equilibrium pressure (MPa)
P_{ft}	Filter tube pressure (MPa)
Q	Mass flow rate of cooling water (kg/s)
T	Temperature (K)
T_{in}	Inlet temperature of cooling water (K)

$\mathbf{u_g}$	Flow velocity of hydrogen (m/s)
$\mathbf{u_f}$	Flow velocity of cooling water (m/s)
X	Reaction fraction (-)

Greek symbols

δ	Baffle cut (-)
δ_f	Fin thickness (mm)
ΔH	Absorption reaction enthalpy (kJ/mol)
ρ	Density (kg/m^3)
λ	Thermal conductivity (W/m/K)
μ	Dynamic viscosity (Pa·s)

Abbreviation

CF	Corrugated fin
CMPENG	Metal hydride compact with expanded natural graphite
CMPGF	Metal hydride compact with graphite flake
DF	Disk fin
DG	Diagonal baffle
EG	Expanded graphite
HL	Hole baffle
MH	Metal hydride
SG	Segmental baffle

1. Introduction

Hydrogen-oxygen fuel cell technology has attracted significant interest worldwide, due to its ambient operating temperature, high energy density, and environmental friendliness. It is considered a promising technology for addressing growing energy and environmental problems [1-3]. But, there are still some challenges for its wide implementation in the electric forklift. One of the most significant obstacles is the compact storage of hydrogen [4-6], as the placement of the fuel cell leaves a small space to the hydrogen storage system. Metal hydride (MH) hydrogen storage method has the characteristics of high volumetric storage capability and safety, which provides a feasible method to solve this problem. Lototskyy et al. [7] tested the commercial 3-tonne fuel cell electric forklift equipped with the MH hydrogen storage tank. The results showed that the electric forklift with the integrated MH tank could continuously operate for 3.1 and 7.25 hours in heavy-duty and light-duty operation. The application of MH hydrogen storage tank in the fuel cell electric forklifts is feasible.

Generally, the low weight storage capacity of metal hydride is a major disadvantage to their use in onboard hydrogen storage. As for material handling forklifts, ballast must be used for keeping balance and steady, and then MH devices could serve as the ballast as well as hydrogen storage system simultaneously. The overall performance of fuel cell electric forklift with integrated MH tank is limited by slow hydrogen charging and discharging of MH tank, as a result of poor heat transfer in MH bed. The intensification of the heat transfer between the MH bed and the cooling water is significant for increasing storage capacity and minimizing refueling time. Yartys et al. [8] reviewed the development of advanced MH hydrogen storage tanks in fuel cell electric forklifts. The improved heat transfer performance of MH tanks can be achieved by adding copper fins or expanded graphite (EG) into the MH bed, and/or by increasing the cooling water flow rate in the external jacket.

Adding copper fins or expanded graphite into the MH bed has been investigated by many researchers in the literature [9-16]. Souahlia et al. [9] experimentally studied the hydrogen storage performance in the MH tank with a finned tube heat exchanger. They compared the refueling time of 4 g hydrogen in cases with or without fins. To

absorb 4 g hydrogen, the tanks without fins and with fins took 3700 s and 1200 s, respectively. Singh et al. [10] extended the conventional heat exchangers [11] by presenting a novel fin design inserted with copper flakes. It was found that the refueling time for reaching hydrogen storage capacity of 1.2 wt % was decreased by 11 % compared to that without copper flakes. Tarasov et al. [12] investigated the MH tank in the form of MH+EG compacts with copper fins. It was observed that the MH tank could reach the hydrogen storage capacity of 20 Nm^3, and provide a stable hydrogen supply for the fuel cell. Davis et al. [13] developed the cassette-type MH tank with internal copper fins and external aluminum fins. They experimentally determined that the combined fin design significantly affected the hydrogen refueling process. The time for reaching 87.5 % hydrogen saturation level is about 4200 s. Chandra et al. [14] conducted numerical simulations on the MH tank, which consists of conical fins and cooling tubes. Due to the large heat transfer area provided by conical fins, the novel system filled with 25 kg $LaNi_5$ only took 1250 s to reach 90 % saturation.

Despite this, there is still room for improvement in refueling time, stability, and cost of MH hydrogen storage tanks for electric forklifts. The optimization of hydrogen storage performance can be conducted by changing the tube side and the shell side of MH tank simultaneously. In this work, the MH hydrogen storage tanks filled with novel AB_5 alloy, as illustrated in Fig. 1, were investigated using the finite element method. We focused on the refueling process in the MH tanks with the combination of tube-side copper fins and shell-side baffles. The influences of device configuration and cooling water flow rate on the refueling time were analyzed. Increasing the cooling water flow rate has been considered an effective heat transfer method in the literature [17-19]. Raju et al. [18] found that the refueling time for reaching 1.03 wt% saturation level decreased by 28.4% with increasing the cooling water flow rate from 0.16 kg/s to 0.32 kg/s. But, the operation methodology about the flow rate of cooling water is still a knowledge gap in existing work. Based on this, we proposed a set of dimensionless parameters that characterize the heat transfer and water flow in the MH tank. We plan to quantify the refueling process in the MH tanks by establishing the correlation between the dimensionless parameters.

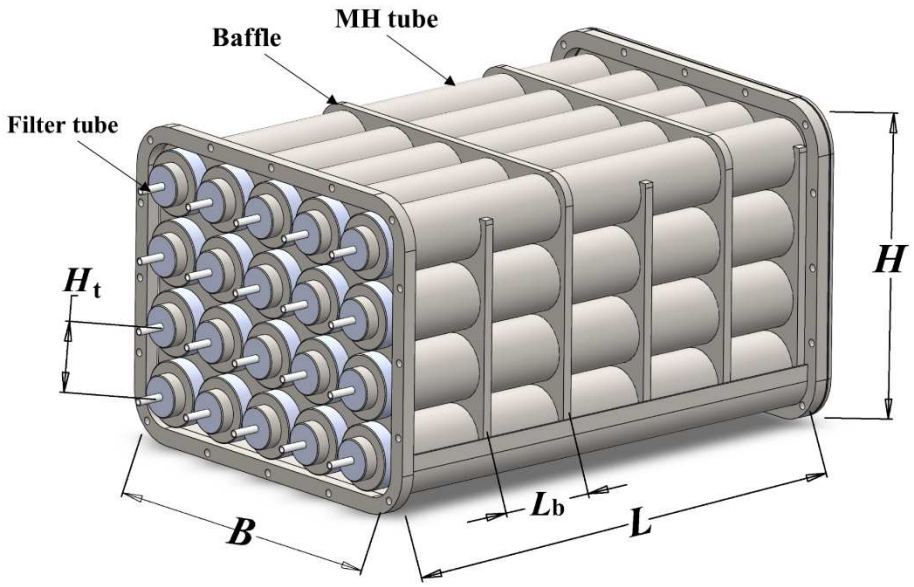

Fig. 1 Schematic diagram of MH hydrogen storage tank for fuel cell electric forklift.

This article is organized in the following manner: in the next section, we discuss the numerical model, including the MH tube configuration, baffle layout, and governing equations. Then, the numerical details adopted in this paper are described briefly with references. Subsequently, in the "Result and discussion" section, we firstly introduce the hydrogen storage properties of AB_5 alloy based on experimental and simulated results. Secondly, we validate the simulation models using the finite element method. Thirdly, we investigate heat and mass transfer intensification on the tube and shell sides of MH tanks. The effect of cooling water flow rate on the hydrogen refueling time is described by the dimensionless correlation $\mathrm{Fo} = \alpha \mathrm{Re}^{\beta}$ (the Fourier number Fo and Reynolds number Re are defined in the next section). The last section provides the conclusions.

2. Simulation

2.1 Hydrogen storage tank configuration

2.1.1 Geometry of metal hydride tube

Fig. 2 shows one of the MH tubes arranged in the shell side of a hydrogen storage tank. It contains a cylindrical tank, a central filter tube made of stainless steel, and several copper fins equally spaced in *z* direction. Two types of copper fins with thickness 4 mm, namely disk fins (DF) and corrugated fins (CF), have been investigated, see the bottom panel of Fig. 2. About 6 kg metal hydride compacts with graphite flake (CMPGF) or with expanded natural graphite (CMPENG) are loaded into the MH tube. Table 1 presents the parameters of the MH tube.

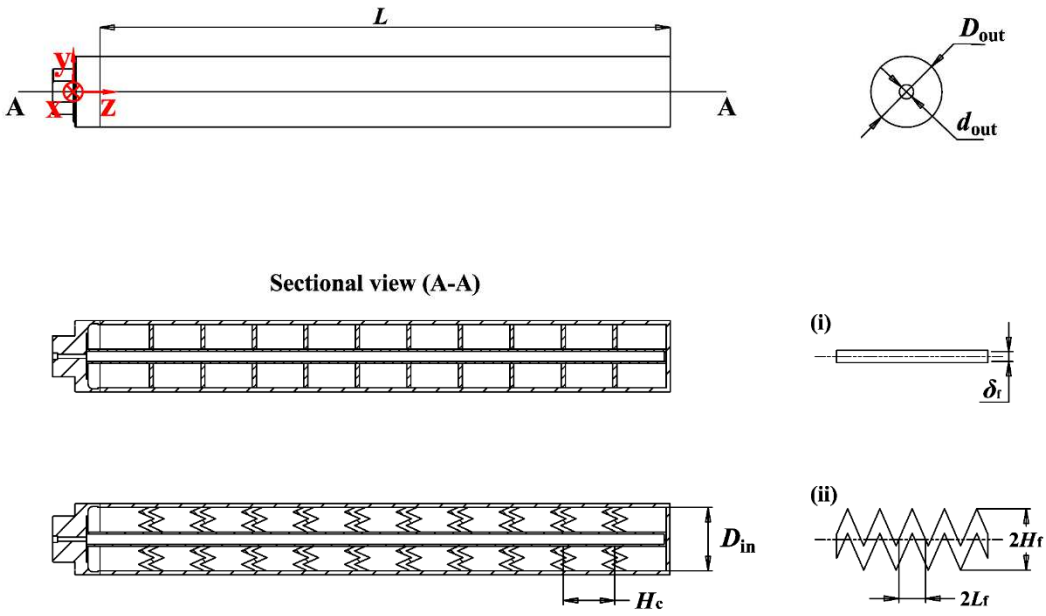

Fig. 2 Geometry of MH tube with (i) disk fins (DF), (ii) corrugated fins (CF) in the tank.

Table 1. Dimensions of the MH hydrogen storage tank

Geometric parameters	Symbol	value
MH tank height (mm)	H	260
MH tank width (mm)	B	330
MH tank length (mm)	L	506
Inner diameter of MH tube (mm)	D_{in}	52
Outer diameter of MH tube (mm)	D_{out}	60
MH tube spacing (mm)	H_t	65
Outer diameter of filter tube (mm)	d_{out}	12
Fin thickness (mm)	δ_f	4
Corrugated fin height (mm)	H_f	12.5
Corrugated fin length (mm)	L_f	5

		.5
Metal hydride compact thickness	H	4
(mm)	$_c$	6
Baffle spacing (mm)	L_b	9 2
Baffle cut (-)	δ	6 %

2.1.2 Geometry of shell-side baffle

Configurations of the MH tanks with segmental baffles (SG), diagonal baffles (DG) and hole baffles (HL) are shown in Fig. 3. Six baffles with thickness 10 mm are equally set in the shell side of the MH tank, and twenty MH tubes are installed in a square arrangement. The baffle cut of SG, DG and HL is set as 6%, which is defined as the ratio of baffle cutting area to shell tube cross-sectional area. The cooling water flows across the baffle cut in the shell side to exchange the reaction heat generated in the MH tube. All geometric parameters of the baffles are listed in Table 1.

(a)

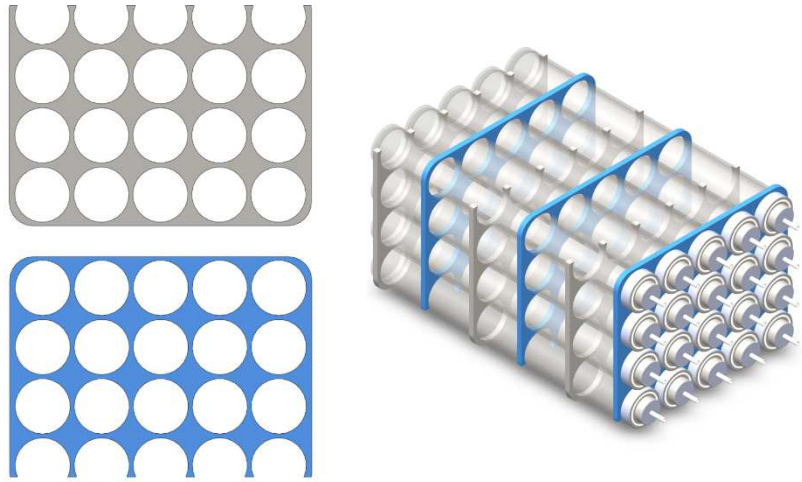

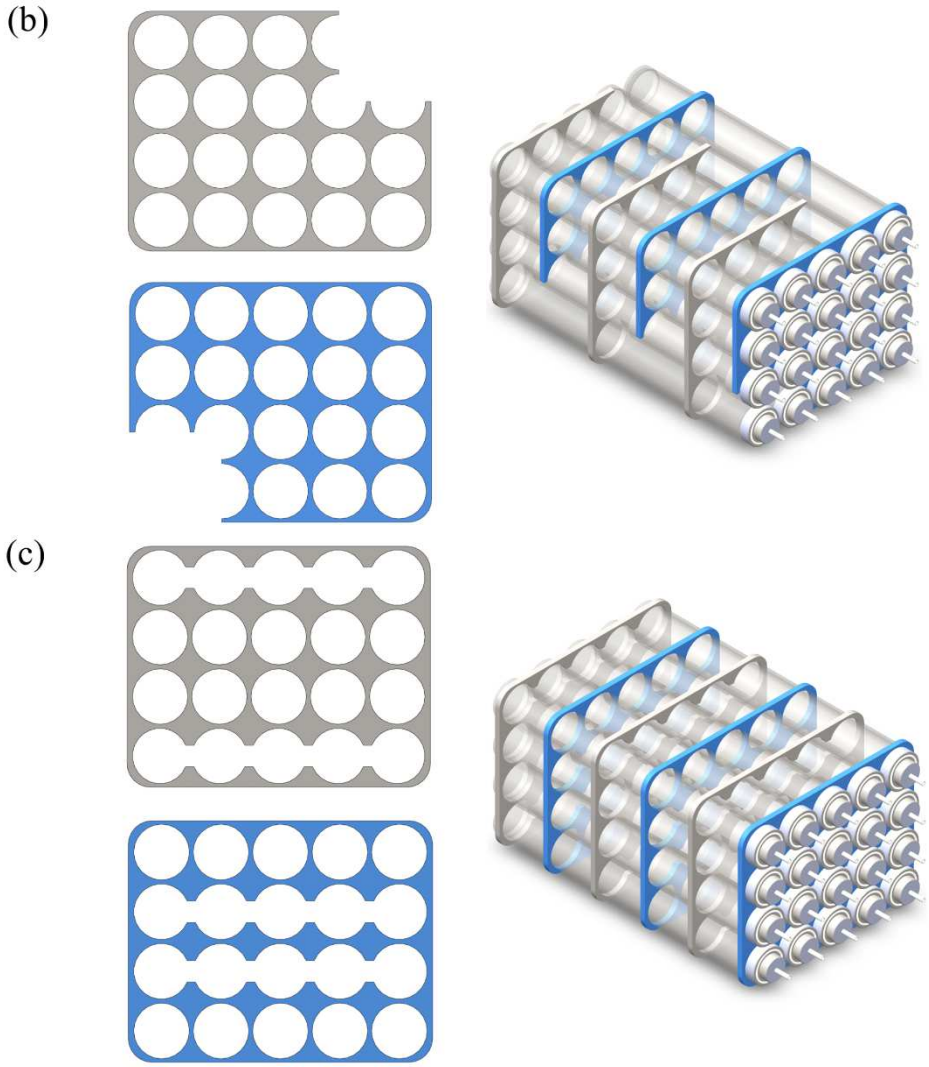

Fig. 3 Geometry of MH hydrogen storage tanks with (a) segmental baffles (SG), (b) diagonal baffles (DG), (c) hole baffles (HL). Baffles with different orientations, indicated in different colors (see the left column), are alternately mounted on the shell side of the MH tank (see the right column).

2.2 Governing equations

The hydrogen flow, absorption reaction and heat transfer are found in the MH bed during the hydrogen storage process. The MH bed is considered as homogeneous and isotropic porous medium with constant thermophysical properties. The hydrogen flow is determined by Darcy's law of an ideal gas. The heat transfer in the MH bed is assumed as a local thermal equilibrium process, and thermal radiation in the bed is ignored [20-23].

Mass conservation for hydrogen in the MH bed can be presented as follows:

$$\varepsilon_{\mathrm{b}}\frac{\partial \rho_{\mathrm{g}}}{\partial t}+\nabla\left(\rho_{\mathrm{g}}\mathbf{u_g}\right)=(1-\varepsilon_{\mathrm{b}})\left(\rho_{\mathrm{sat}}-\rho_{\mathrm{alloy}}\right)\frac{dX}{dt} \tag{1}$$

where, ρ_{g} and $\mathbf{u_g}$ are the density and flow velocity of hydrogen, respectively; ρ_{alloy} and ρ_{sat} are the initial density and saturated density of MH, respectively; ε_{b} is the porosity of the MH bed; dX/dt is the hydrogen absorption rate.

The hydrogen velocity $\mathbf{u_g}$ is described by Darcy's law:

$$\mathbf{u_g}=-\frac{K}{\mu_{\mathrm{g}}}\nabla P \tag{2}$$

where, P and μ_{g} are the pressure and dynamic viscosity of hydrogen, respectively; The permeability K is calculated by the Kozeny-Carman equation $K=\frac{d_p^2\varepsilon_b^3}{150(1-\varepsilon_b)^2}$ with d_{p} the metal particle diameter.

Energy conservation for MH bed can be written as follows:

$$\left(\rho C_{\mathrm{p}}\right)_{\mathrm{e}}\frac{\partial T}{\partial t}+\rho_{\mathrm{g}}C_{\mathrm{pg}}\mathbf{u_g}\nabla T=\lambda_{\mathrm{e}}\nabla^2 T+\frac{\Delta \mathrm{H}}{M_{\mathrm{g}}}(1-\varepsilon_{\mathrm{b}})\left(\rho_{\mathrm{sat}}-\rho_{\mathrm{alloy}}\right)\frac{dX}{dt} \tag{3}$$

where, T is the effective temperature of MH and hydrogen; $\Delta \mathrm{H}$ is the absorption reaction enthalpy; C_{pg} and M_{g} are the specific heat capacity and molecular mass of hydrogen, respectively; $(\rho C_{\mathrm{p}})_{\mathrm{e}}$ and λ_{e} are the effective heat capacity and thermal conductivity, respectively, which can be obtained:

$$\left(\rho C_{\mathrm{p}}\right)_{\mathrm{e}}=\varepsilon_{\mathrm{b}}\rho_{\mathrm{g}}C_{\mathrm{pg}}+(1-\varepsilon_{\mathrm{b}})\rho C_{\mathrm{p}} \tag{4}$$

$$\lambda_{\mathrm{e}}=\varepsilon_{\mathrm{b}}\lambda_{\mathrm{g}}+(1-\varepsilon_{\mathrm{b}})\lambda \tag{5}$$

where, ρ and C_{p} are the density and specific heat capacity of MH, respectively; λ and λ_{g} are the thermal conductivity of MH and H_2, respectively.

Energy conservation for copper fins can be formulated as follows:

$$\rho_{\mathrm{fin}}C_{\mathrm{pfin}}\frac{\partial T_{\mathrm{fin}}}{\partial t}=\lambda_{\mathrm{fin}}\nabla^2 T_{\mathrm{fin}} \tag{6}$$

where, T_{fin} and λ_{fin} are the temperature and thermal conductivity of fins, respectively; ρ_{fin} and C_{pfin} are the density and specific heat capacity of fins, respectively.

Energy conservation for cooling water can be presented as follows:

$$\rho_{\mathrm{f}}C_{\mathrm{pf}}\frac{\partial T_{\mathrm{f}}}{\partial t}+\rho_{\mathrm{f}}C_{\mathrm{pf}}\mathbf{u_f}\nabla T_{\mathrm{f}}=\lambda_{\mathrm{f}}\nabla^2 T_{\mathrm{f}} \tag{7}$$

where, T_f, $\mathbf{u_f}$ and λ_f are the temperature, velocity and thermal conductivity of cooling water, respectively; ρ_f and C_{pf} are the density and specific heat capacity of cooling water, respectively.

The Reynolds number of cooling water in the MH tanks with different baffles can be calculated:

For segmental baffles or diagonal baffles [24]:

$$u = \frac{Q}{\rho_f (B - N_c D_{out}) L_b} \tag{8}$$

$$\mathrm{Re} = \frac{\rho_f u D_{out}}{\mu_f} \tag{9}$$

where, Q is the mass flow rate of cooling water; N_c is the number of MH tubes in the central row; μ_f is the dynamic viscosity of cooling water;

For hole baffles [25]:

$$\mathrm{Re} = \frac{4Q}{\mu_f \pi [2(B + H) + N_t D_{out}]} \tag{10}$$

where, N_t is the total number of MH tubes in the MH tank.

Note that it is illustrated that the shell side flow is fully developed turbulent for Re>100 in shell and tube tank [25, 26]. In this study, the Reynolds numbers are greater than 100. Realizable *k-ε* model is used to solve the turbulent flow of cooling water in the shell side of the MH tank, because of its superior performance to the standard *k-ε* model for the flow involving rotation and bypass [27, 28].

2.3 Numerical details

Based on the mentioned above, the MH tanks with different combined configurations were simulated by using the finite element method. Three simulation domains were defined, one solid domain which is metal hydride bed in the MH tube, and two fluid domains which are hydrogen in the MH tube and cooling water in the shell side of the MH tank. The thickness of the MH tubes is neglected in the simulations for simplifying the grid numbers. Table 2 lists the parameters of the materials adopted in this study.

Table 2. Thermodynamic parameters of materials

Parameters	Alloy	Hydrogen	Copper	Water
Initial density, ρ_{alloy} (kg/m^3)	8200	-	8700	1000
Saturated density, ρ_{sat} (kg/m^3)	8328	-	-	-
Specific heat capacity, C_p (J/kg/K)	419	14890	385	4183
Thermal conductivity of CMPGF, λ (W/m/K)	4.7	0.22	400	0.5989
Thermal conductivity of CMPENG, λ (W/m/K)	7.2	-	-	-
Porosity, ε_b (-)	0.3	-	-	-
Metal powder diameter, d_p (μm)	28.3	-	-	-
Initial temperature, T_i (K)	293	293	293	293
Initial pressure, P_i (MPa)	4	4	-	-

The inlet temperature of cooling water was considered as the initial temperature of T_{in}=T_i=293 K. The pressure in the hydrogen filter tube was set as the initial pressure of P_{ft}=P_i=4 MPa. The wall of the MH tank was thermal insulating and non-flowing. The heat transfer rate between the MH bed and the cooling water was $q_0 = h_0(T - T_f)$ with h_0 set as 1000 W/m^2/K. The commercial software COMOSL was adopted to simulate the hydrogen refueling process in the computational domains. The segregated solver was used for solving the governing equations with the implicit time-stepping method for time advancement. The simulations reached convergence as the relative tolerance 10^{-3} and absolute tolerance 10^{-4}.

Fig.4 shows the gird independence tests for CMPGF-DF-SG. Three groups of test grids are composed of 1.0 million, 2.4 million and 3.6 million grids, respectively. The good agreement in terms of average bed temperature and average bed storage capacity is demonstrated by using the middle and fine grids. Therefore, the system with 2.4 million grids was selected to investigate the hydrogen refueling process in the MH tanks.

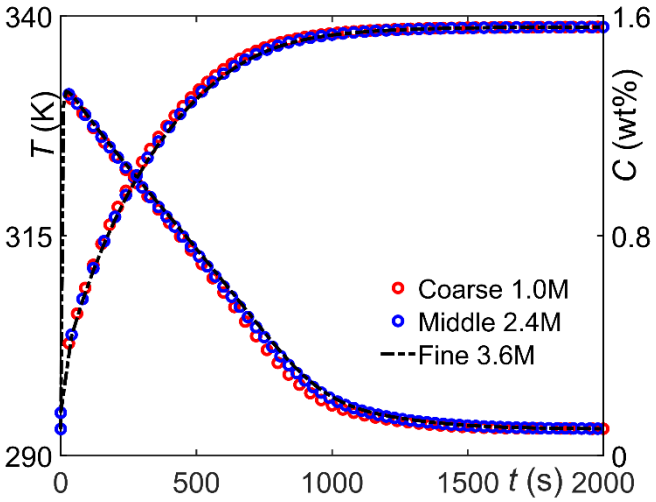

Fig. 4 Effect of grids on average bed temperature and average bed storage capacity for CMPGF-DF-SG at P_{ft}=4 MPa, T_{in}=293 K and Q=0.5 kg/s.

3. Result and discussion

3.1 Metal hydride material

3.1.1 Thermodynamic equilibrium pressure

Metal hydride used in this study is based on the AB_5-type hydrogen storage alloy manufactured by our co-authors from GRINM Group Co., Ltd. The novelty of this alloy is their moderate equilibrium pressure for electric forklift application. Fig. 5a shows the pressure-concentration isotherms of the alloy samples at T=293, 313 and 333 K, as well as the polynomial fitting of the isotherms. It can be observed that the metal hydride possesses a maximum hydrogen storage capacity of 1.6 wt%, and a flat equilibrium pressure lower than 4 MPa during operating temperature. The results indicate that the MH tank filled with the metal hydride can absorb the same mass of hydrogen as the separate compressed H_2 composite cylinder charged at P=35 MPa, but at lower hydrogen supply pressure (<4 MPa) and lower tank volume. In Fig. 5b, it can be found that the heat generated in the refueling process is minimized due to the low reaction enthalpy ΔH=-26 kJ/mol, calculated by using the van't Hoff equation [29]. Meanwhile, the reaction entropy change ΔS is found to be 205 J/mol/K.

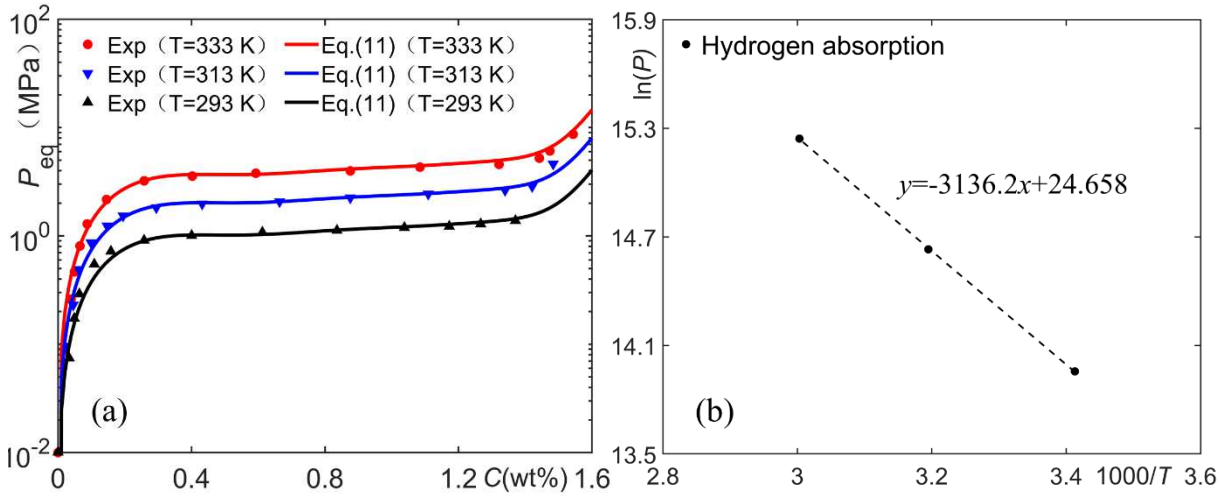

Fig. 5 Thermodynamic data of AB_5 alloy (a) pressure-concentration isotherms (PCT) (b) van't Hoff plot.

The Eq. (11) is the polynomial function [30-32] of the experimental equilibrium pressure (P_{eq}). The nine-order coefficients a_i are presented in Table 3. The deviation between the fitting data and the experimental data can be ignored, see Fig. 5a.

$$P_{eq} = \sum_{i=0}^{n} a_i C^i \exp\left(\frac{\Delta H}{R_g}\left(\frac{1}{T} - \frac{1}{T_0}\right)\right) \quad (11)$$

where, C(wt %) denotes the weight percentage of absorbed hydrogen and metal hydride; R_g and T_0 are the ideal gas constant and reference temperature 333 K, respectively.

Table 3. Coefficients of the nine-order equilibrium pressure polynomial function

Coefficients (MPa)	a_0	a_1	a_2	a_3	a_4	a_5	a_6	a_7	a_8	a_9
	$2.529e^{-10}$	7.754	103.3	-547.9	1070	-867.8	-0.7761	486.4	-309.5	62.84

3.1.2 Absorption kinetic equation

The absorption kinetic equation of metal hydride can be written as the following Eq. (12) [33]:

$$\frac{dX}{dt} = C_{\mathrm{a}} \exp\left(-\frac{E_{\mathrm{a}}}{R_{\mathrm{g}}T}\right) \ln\left(\frac{P}{P_{\mathrm{eq}}}\right)(1-X) \tag{12}$$

where, X indicates the fraction of the absorption reaction; C_{a} and E_{a} are the reaction constant 59.1 1/s and activation energy 21.17 kJ/mol, respectively.

Fig. 6 shows the comparison of absorption kinetics between the experimental and simulated results. The kinetic experiments were performed using a Sieverts-type apparatus (GRINM, China). The lab-scale reactor was submerged in a bath in which the temperature is controlled at 293 K. The hydrogen pressure was set as 6 MPa. It can be found that the simulated results, solved by Eq. (12), are in good agreement with the experimental results. For instance, the experimental saturation time of hydrogen storage is 425 s, and the simulated saturation time is 432 s. The alloy shows fast absorption kinetics, which is beneficial to improving hydrogen refueling time for MH tanks. In the next section, the Fourier number is defined $F_o = \lambda t_{1.5\mathrm{wt\%}}/\rho C_{\mathrm{p}} D_{in}^2$ with $t_{1.5\mathrm{wt\%}}$ the refueling time for reaching 1.5 wt% saturation level. We plan to use the dimensionless refueling time to characterize the hydrogen storage efficiency in MH tanks, and investigate the effect of cooling water flow rate on the hydrogen refueling process.

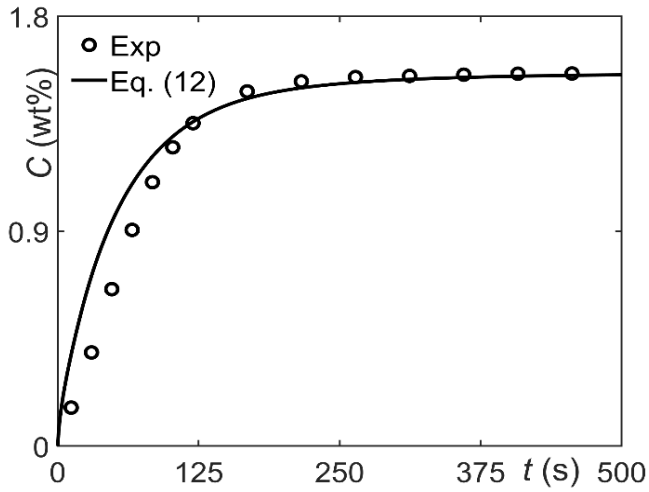

Fig. 6 Absorption of AB_5 alloy at P=6 MPa and T=293 K.

3.2 Model validation of MH tank

We verified our mathematical models by simulating the hydrogen refueling process inside the cylindrical tank studied by Singh et al. [34]. The tank structure and operating conditions were kept the same as the work [34]. The average bed temperature and average bed storage capacity during the hydrogen storage process are shown in Fig. 7. Clearly, the present simulated bed temperature matches quite well with the experimental data [34], better than the simulated data in the work [34], see Fig. 7a. The time history of average bed storage capacity obtained by the present simulation is in reasonable agreement with the experimental data of Singh et al. [34], as illustrated in Fig. 7b. The results show that the saturation time in our simulation and the literature is consistent.

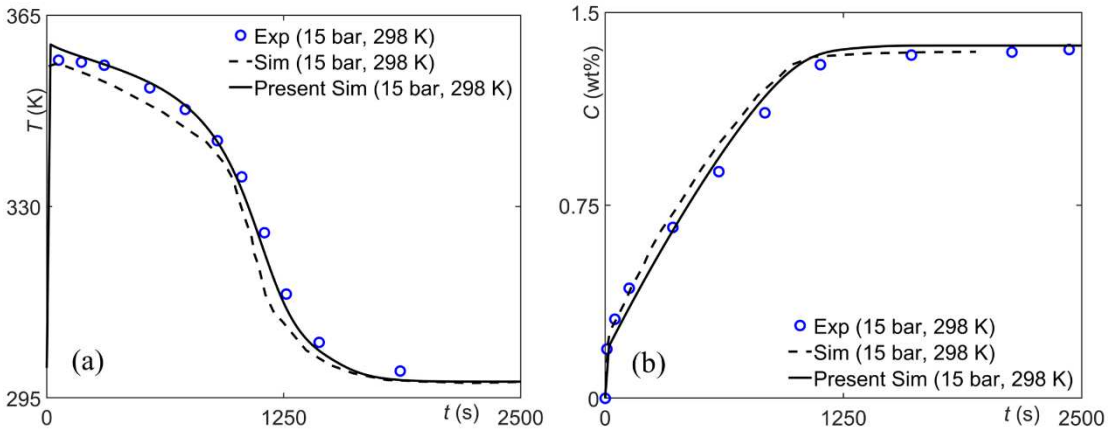

Fig. 7 Model validation with literature data from Singh et al. [34] (a) average bed temperature, (b) average bed storage capacity.

3.3 Intensification on the tube side of MH tank

In this section, the hydrogen refueling processes in the CMPGF-DF-SG, CMPGF-CF-SG and CMPENG-CF-SG were studied. The operating conditions were set as P_{ft}=4 MPa, T_{in}=293 K and Q=0.5 kg/s.

Fig. 8 shows the time histories of average bed temperature and average bed storage capacity in the three types of tube-side intensification design. It is obvious that the improvement of hydrogen storage performance is present in the CMPGF-CF-SG and CMPENG-CF-SG. Compared with the CMPGF-DF-SG, the cooling time to reach the average bed temperature of 300 K is reduced by 16% and 30% in the CMPGF-CF-SG and

CMPENG-CF-SG, respectively, see Fig. 8a. The heat transfer in MH tanks with tube-side corrugated fins is faster than that with tube-side disk fins. In Fig. 8b, the refueling time to reach 1.5 wt% saturation level is found to be 830 s in the CMPGF-DF-SG, while the CMPGF-CF-SG and CMPENG-CF-SG only 730 s and 630 s, respectively. It should be noted that the refueling time in the CMPGF-CF-SG or CMPENG-CF-SG is less than that of MH tanks in the literature [17, 35, 36]. Our MH tank with tube-side intensification design can provide two kilograms of hydrogen after 10 minutes of hydrogen charging.

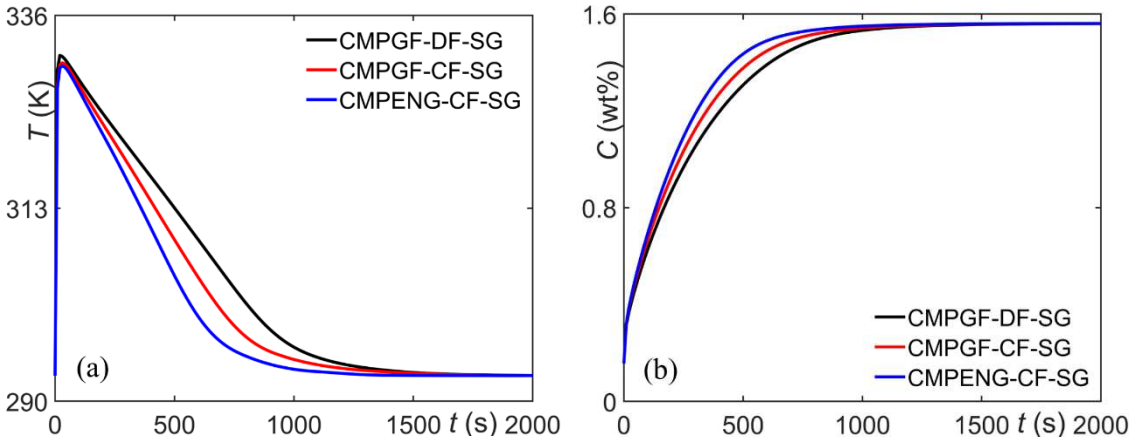

Fig. 8 Comparison of three MH tube configurations (a) time history of average bed temperature, (b) time history of average bed storage capacity at P_{ft}=4 MPa, T_{in}=293 K and Q=0.5 kg/s.

Fig. 9 shows the simulated bed storage capacity distribution for three MH tube configurations. It can be seen there are two reaction fronts in the MH tubes, demarcating the saturation regions from the rest of the unsaturation regions. One moves from the surrounding area of the tube wall to the interior of the MH tube, and the other starts in the region of copper fins and moves to the neighboring fins. As the corrugated fins could provide a large thermal contact surface, the hydrogen storage performance of CMPGF-CF-SG and CMPENG-CF-SG is much better than that of CMPGF-DF-SG. Furthermore, the variation of bed storage capacity in z direction is clearly demonstrated, see snapshots t=600 s. We can find that the bed storage capacity in MH tubes decreases with the negative direction of z-axis, in accordance with the flow direction of cooling

water. This is because the cooling water takes reaction heat generated by the MH bed, leading to the decrease of temperature difference between the MH bed and the cooling water, thus reducing the driving force of heat transfer along the flow direction.

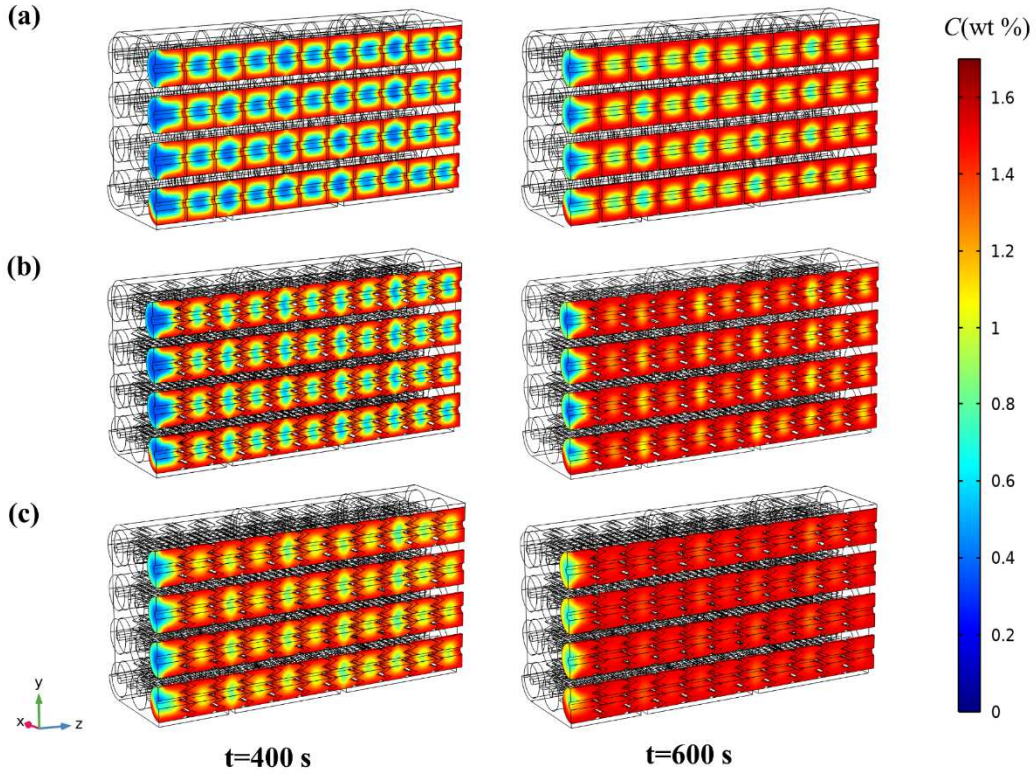

Fig. 9 Distribution of bed storage capacity in three MH tube configurations (a) CMPGF-DF-SG, (b) CMPGF-CF-SG, (c) CMPENG-CF-SG at P_{ft}=4 MPa, T_{in}=293 K and Q=0.5 kg/s.

3.4 Intensification on the shell side of MH tank

In this section, the influence of shell-side baffle design on the hydrogen refueling process was investigated. The MH tanks with segmental baffles, diagonal baffles and hole baffles were named CMPGF-CF-SG, CMPGF-CF-DG and CMPGF-CF-HL, respectively. The operating conditions were set as P_{ft}=4 MPa, T_{in}=293 K.

3.4.1 Simulated flow field

Fig. 10 shows the streamlines and velocity distribution of cooling water in the shell side of the CMPGF-CF-SG, CMPGF-CF-DG and CMPGF-CF-HL. Based on the turbulent criterion mentioned in Section 2.2,

we consider the flow with Q=0.5 kg/s and Re=4037 is turbulent. It is found that the flow characteristics in the shell side of MH tank are dependent on baffle design. In Fig. 10a, the zigzag flow pattern is present in the CMPGF-CF-SG. Adjacent segmental baffles form five shell-side chambers, in which the cooling water passes through the MH tubes close to a vertical pattern. It is noted that a helical flow pattern appears in the CMPGF-CF-DG, as shown in Fig.10b. Due to the effect of helical flow, the dead flow zone in the shell side of the MH tank decreases obviously. The flow velocity of cooling water in the CMPGF-CF-DG is found to be the highest, compared with the CMPGF-CF-SG and CMPGF-CF-HL. Thus, it can be deduced preliminarily that the heat transfer in the CMPGF-CF-DG could be the best one among the three baffle designs.

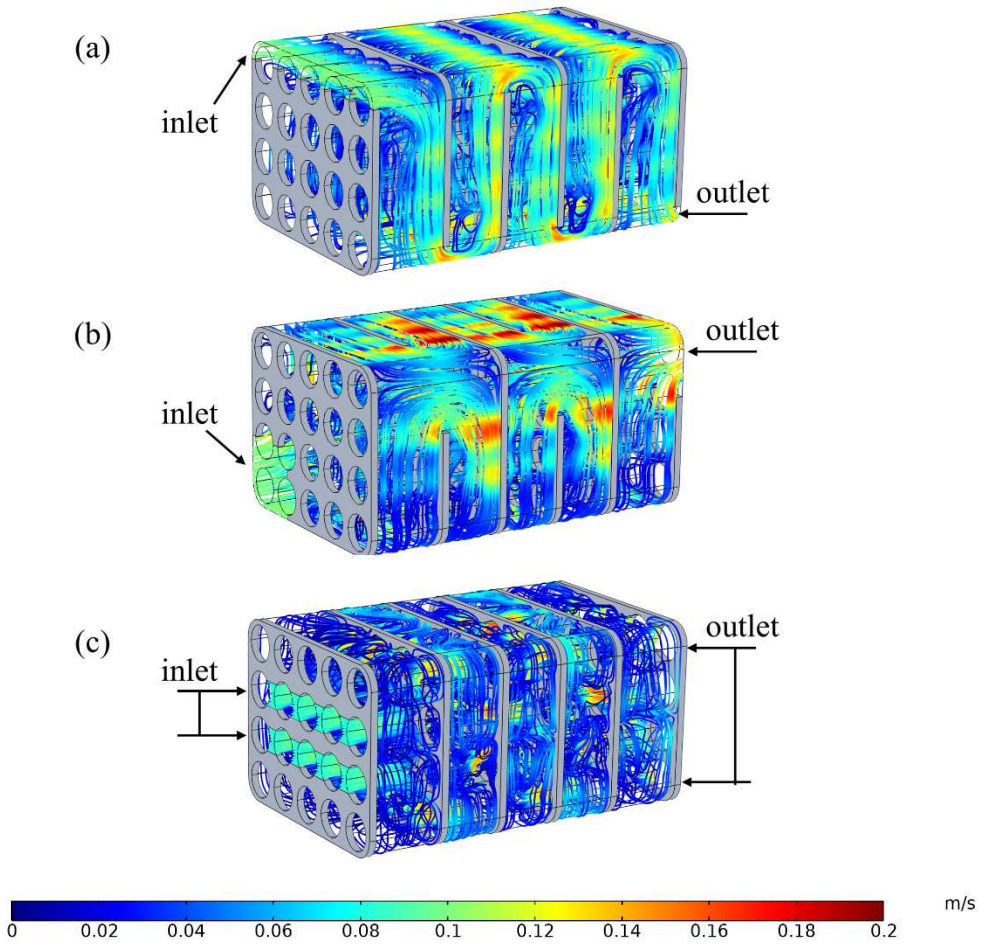

Fig. 10 Streamlines and velocity distribution of cooling water in MH tanks with (a) segmental baffles, (b) diagonal baffles, (c) hole baffles at P_{ft}=4 MPa, T_{in}=293 K and Q=0.5 kg/s.

Fig. 10c shows the flow pattern in the CMPGF-CF-HL. It can be observed that the plug flow is induced and MH tube bundles are scoured by the high velocity jet fluid. The maximum velocity of cooling water is slightly higher than the conventional segmental baffle design, due to the enhanced scour caused by the high-velocity jet.

3.4.2 Simulated refueling time

Fig. 11 shows the comparison of the refueling time in the CMPGF-CF-SG, CMPGF-CF-DG and CMPGF-CF-HL. It can be found that the refueling time in MH tanks with three baffle designs decreases with the increase of cooling water flow rate. As Q increased from 0.09 kg/s to 2 kg/s, the experimental refueling time in the CMPGF-CF-DG decreased from 880 s to 690 s, and the simulated time decreased from 800 s to 648 s, that is, the simulated results are in good agreement with the experimental data. The maximum deviation between the simulated results and experimental data in the CMPGF-CF-DG is 9.1% at lowest Q, and the deviation decreases to 6.1% at highest Q. As for the discrepancy between the simulated and experimental data, one reason might be the thin-wall assumption for the MH tube wall. Another reason might be that single turbulence model was used for various Q, because the model provides better prediction at high Q in comparison with that at low Q.

Moreover, $t_{1.5wt\%}$ the simulated refueling time in the CMPGF-CF-DG is found to be shorter than those in the CMPGF-CF-SG and the CMPGF-CF-HL at Q=0.5-2 kg/s, as shown in Fig.11. This is because the diagonal baffle design produces a higher velocity of cooling water, resulting in the notable thermal intensification in the shell side of the MH tank.

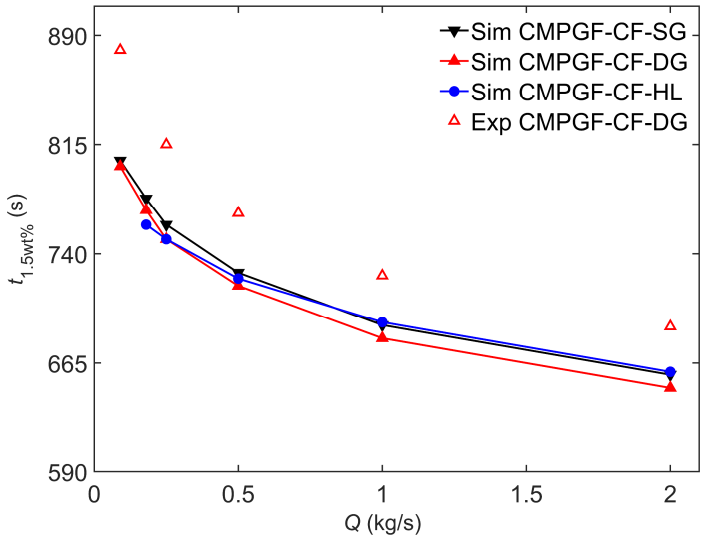

Fig. 11 Simulated and experimental refueling time in different MH hydrogen storage tanks at P_{ft}=4 MPa, T_{in}=293 K and Q=0.09, 0.18, 0.25, 0.5, 1, 2 kg/s.

However, there is a different order for the refueling time when the mass flow rate decreases to Q=0.18 kg/s. We can find the simulated refueling time in the CMPGF-CF-SG, CMPGF-CF-DG and CMPGF-CF-HL is 778, 770 and 760 s, respectively, where the $t_{1.5wt\%}$ in the CMPGF-CF-HL is the shortest. To address the mechanism of this variation, the heat transfer process in the MH tanks was analyzed, as shown in Fig.12. It is evident that the outlet temperature of cooling water in the CMPGF-CF-HL is lower than those in the CMPGF-CF-SG and CMPGF-CF-DG. This means the high temperature difference between the MH bed and the cooling water is present in the CMPGF-CF-HL, which increases the driving force for heat transfer. As shown in Fig.12b, the high driving force for heat transfer is clearly seen in the last two chambers of CMPGF-CF-HL. It happens because the flow pattern in the CMPGF-CF-HL is more inclined to be the plug flow, which can take away the high-temperature water of the last two chambers more quickly. In contrast, the fluid recirculation and dead zone in the CMPGF-CF-SG and CMPGF-CF-DG would promote the backmixing of cooling water at different temperature, thus reducing the heat transfer in the MH tank. Based on this, the plug flow pattern in MH tank is considered to be a better flow pattern at the operating condition of low cooling water mass flow rate.

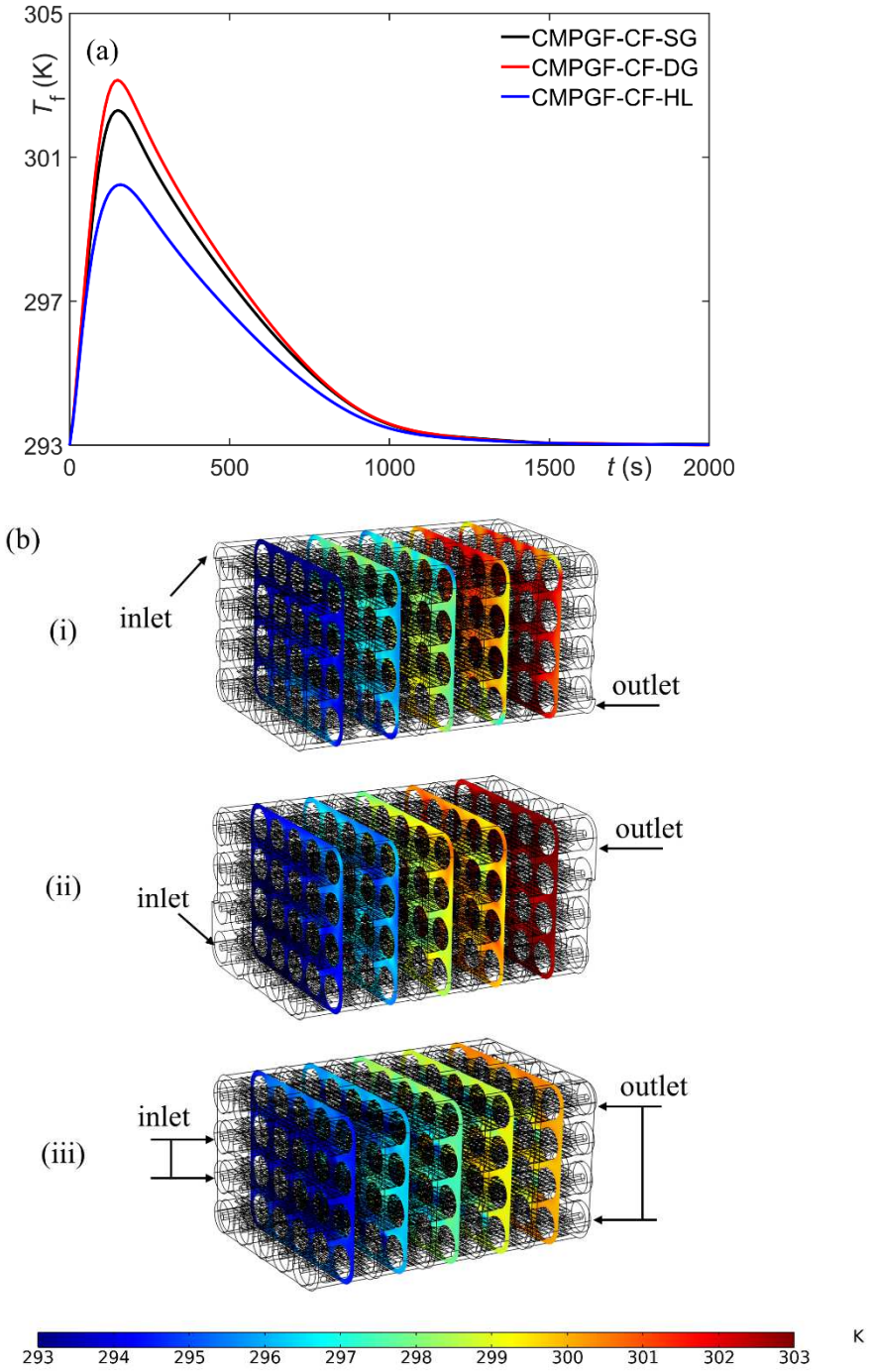

Fig. 12 Variation in cooling water temperature at Q=0.18 kg/s (a) time history of outlet temperature (b) temperature distribution in MH tanks at t=200 s: (i) CMPGF-CF-SG, (ii) CMPGF-CF-DG, (iii) CMPGF-CF-HL.

3.4.3 Establishment of correlation

Fig. 13 shows the relationship between Fourier number and Reynolds number in three types of MH hydrogen storage tank. It can be found that the Fo decreases with increasing Re, and the decrease in Fo is most significant in the CMPGF-CF-DG. We established the correlation (13) between Fo and Re to quantify the effect of cooling water flow rate on the hydrogen refueling time, see the dotted line in Fig. 13. The regression results are in good agreement with the numerical data, and the correlation coefficients are shown in Table 4.

$$\mathrm{Fo} = \alpha \mathrm{Re}^{\beta} \tag{13}$$

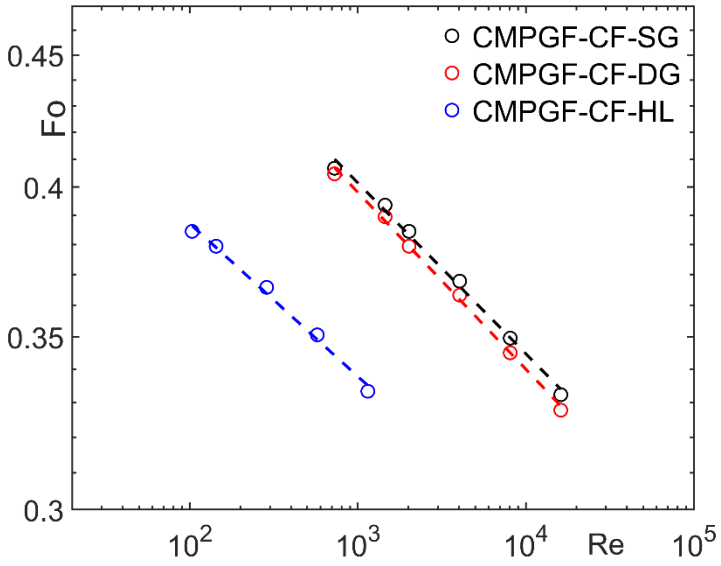

Fig. 13 Correlation between Fourier number and Reynolds number for different MH hydrogen storage tanks.

Table 4 shows that the exponents of Re are negative in three MH tanks, and the absolute values of factors α and β are both smaller in the CMPGF-CF-HL. It indicates that the CMPGF-CF-HL are expected to provide the shortest refueling time in the low Reynolds number, and the effect of Re on the hydrogen refueling process is not obvious in the CMPGF-CF-HL.

Table 4. Regression results of correlation between Fo and Re

MH tank	α	β	R^2
CMPGF-CF-SG	0.6343	-0.0662	0.9950
CMPGF-CF-DG	0.6390	-0.0685	0.9976
CMPGF-CF-HL	0.5085	-0.0592	0.9927

The following correlations transformed from the above Eq. (13) can be used to evaluate the refueling time in MH tanks. Based on these methodologies, we can adjust the hydrogen refueling performance of the MH tank to meet the application requirements of fuel cell electric forklifts, or choose the optimal configuration and operating condition of the MH tank.

For CMPGF-CF-SG:

$$t_{1.5\text{wt\%}} = 0.6343\frac{\rho C_{\text{p}} D_{\text{in}}^2}{\lambda}\text{Re}^{-0.0662} \quad 726 < \text{Re} < 16149 \tag{14}$$

For CMPGF-CF-DG:

$$t_{1.5\text{wt\%}} = 0.6390\frac{\rho C_{\text{p}} D_{\text{in}}^2}{\lambda}\text{Re}^{-0.0685} \quad 726 < \text{Re} < 16149 \tag{15}$$

For CMPGF-CF-HL:

$$t_{1.5\text{wt\%}} = 0.5085\frac{\rho C_{\text{p}} D_{\text{in}}^2}{\lambda}\text{Re}^{-0.0592} \quad 103 < \text{Re} < 1148 \tag{16}$$

4. Conclusions

In this paper, a series of MH hydrogen storage tanks for fuel cell electric forklifts have been developed. The MH tanks are filled with novel metal hydride manufactured by our co-authors from GRINM Group Co., Ltd., and comprise the tube-side fins and the shell-side baffles. The finite element method is applied to study the hydrogen refueling process in the MH tanks.

Time histories of average bed storage capacity and average bed temperature were predicted in the CMPGF-DF-SG, CMPGF-CF-SG and CMPENG-CF-SG. It is found that the MH tank with tube-side disk fins takes 830 s for reaching 1.5 wt% saturation level, while the CMPGF-CF-SG and CMPENG-CF-SG only 730 s and 630 s. The refueling time in the MH tank with tube-side corrugated fins is less than those in most literature [17, 35, 36].

For intensification on the shell side of MH tanks, we compared the shell side flow field and hydrogen refueling time in MH tanks with different baffles: segmental, diagonal and hole baffles. Simulated flow field in the shell side shows that the flow velocity of cooling water in the CMPGF-CF-DG is higher, compared with the CMPGF-CF-SG and CMPGF-CF-HL. This leads to the best heat transfer performance present in the CMPGF-CF-DG, thus obtaining the shortest refueling time 648 s at Q=2 kg/s, and the simulated refueling time matches well with the experimental data. But, there is an interesting finding that the refueling time sequence is CMPGF-CF-HL< CMPGF-CF-DG< CMPGF-CF-SG, when the Q decreases to 0.18 kg/s. The flow pattern in the CMPGF-CF-HL is more inclined to be the plug flow, which can reduce the backmixing of cooling water.

Based on this, a dimensionless correlation $\mathrm{Fo} = \alpha \mathrm{Re}^{\beta}$ is proposed to describe the effect of cooling water flow rate on the hydrogen refueling time in different MH tanks. The hydrogen storage performance in terms of refueling time in MH tanks can be obtained by the correlations: $t_{1.5\mathrm{wt\%}} = 0.6343 \frac{\rho C_{\mathrm{p}} D_{\mathrm{in}}^2}{\lambda} \mathrm{Re}^{-0.0662}$ for CMPGF-CF-SG, $t_{1.5\mathrm{wt\%}} = 0.6390 \frac{\rho C_{\mathrm{p}} D_{\mathrm{in}}^2}{\lambda} \mathrm{Re}^{-0.0685}$ for CMPGF-CF-DG and $t_{1.5\mathrm{wt\%}} = 0.5085 \frac{\rho C_{\mathrm{p}} D_{\mathrm{in}}^2}{\lambda} \mathrm{Re}^{-0.0592}$ for CMPGF-CF-HL. It could be regarded as the references for the design of MH hydrogen storage tanks in fuel

cell electric forklifts.

References

[1] Pollet BG, Pasupathi S, Swart G, Mouton K, Lototskyy M, Williams M, et al. Hydrogen South Africa (HySA) systems competence centre: mission, objectives, technological achievements and breakthroughs. Int J Hydrog Energy. 2014;39:3577-96.

[2] Abe JO, Popoola API, Ajenifuja E, Popoola OM. Hydrogen energy, economy and storage: Review and recommendation. Int J Hydrogen Energy. 2019;44:15072-86.

[3] Bockris JOM. The origin of ideas on a Hydrogen Economy and its solution to the decay of the environment. Int J Hydrog Energy. 2002;27:731-40.

[4] Hirscher M, Yartys VA, Baricco M, Bellosta von Colbe J, Blanchard D, Bowman RC, et al. Materials for hydrogen-based energy storage-past, recent progress and future outlook. J Alloy Compd. 2020;827:153548.

[5] Lototskyy M, Tolj I, Davids MW, Bujlo P, Smith F, Pollet BG. “Distributed hybrid” MH-CGH_2 system for hydrogen storage and its supply to LT PEMFC power modules. J Alloy Compd. 2015;645:S329-S33.

[6] Keränen TM, Karimäki H, Viitakangas J, Vallet J, Ihonen J, Hyötylä P, et al. Development of integrated fuel cell hybrid power source for electric forklift. J Power Sources. 2011;196:9058-68.

[7] Lototskyy MV, Tolj I, Parsons A, Smith F, Sita C, Linkov V. Performance of electric forklift with low-temperature polymer exchange membrane fuel cell power module and metal hydride hydrogen storage extension tank. J Power Sources. 2016;316:239-50.

[8] Yartys VA, Lototskyy MV, Linkov V, Pasupathi S, Davids MW, Tolj I, et al. HYDRIDE4MOBILITY: an EU HORIZON 2020 project on hydrogen powered fuel cell utility vehicles using metal hydrides in hydrogen storage and refuelling systems. Int J Hydrog Energy. 2021;46:35896-909.

[9] Souahlia A, Dhaou H, Askri F, Mellouli S, Jemni A, Nasrallah SB. Experimental study and characterization of metal hydride containers. Int J Hydrog Energy. 2011;36:4952-7.

[10] Singh A, Maiya MP, Srinivasa Murthy S. Experiments on solid state hydrogen storage device with a finned tube heat exchanger. Int J Hydrog Energy. 2017;42:15226-35.

[11] Satya Sekhar B, Lototskyy M, Kolesnikov A, Moropeng ML, Tarasov BP, Pollet BG. Performance analysis of cylindrical metal hydride beds with various heat exchange options. J Alloy Compd. 2015;645:S89-S95.

[12] Tarasov BP, Fursikov PV, Volodin AA, Bocharnikov MS, Shimkus YY, Kashin AM, et al. Metal hydride hydrogen storage and compression systems for energy storage technologies. Int J Hydrog Energy. 2021;46:13647-57.

[13] Davids MW, Lototskyy M, Malinowski M, van Schalkwyk D, Parsons A, Pasupathi S, et al. Metal hydride hydrogen storage tank for light fuel cell vehicle. Int J Hydrog Energy. 2019;44:29263-72.

[14] Chandra S, Sharma P, Muthukumar P, Tatiparti SSV. Strategies for scaling-up $LaNi_5$-based hydrogen storage system with internal conical fins and cooling tubes. Int J Hydrog Energy. 2021;46:19031-45.

[15] Rizzi P, Pinatel E, Luetto C, Florian P, Graizzaro A, Gagliano S, et al. Integration of a PEM fuel cell with a metal hydride tank for stationary applications. J Alloy Compd. 2015;645:S338-S42.

[16] Heubner F, Mauermann S, Kieback B, Röntzsch L. Stress development of metal hydride composites for high density hydrogen storage applications. J Alloy Compd. 2017;705:176-82.

[17] Lototskyy M, Tolj I, Klochko Y, Davids MW, Swanepoel D, Linkov V. Metal hydride hydrogen storage tank for fuel cell utility vehicles. Int J Hydrog Energy. 2020;45:7958-67.

[18] Raju NN, Muthukumar P, Selvan PV, Malleswararao K. Design methodology and thermal modelling of industrial scale reactor for solid state hydrogen storage. Int J Hydrog Energy. 2019;44:20278-92.

[19] Mathew A, Nadim N, Chandratilleke TT, Humphries TD, Paskevicius M, Buckley CE. Performance analysis of a high-temperature magnesium hydride reactor tank with a helical coil heat exchanger for thermal storage. Int J Hydrog Energy. 2021;46:1038-55.

[20] Shaji S, Mohan G. Numerical simulation of the effect of aluminum foam on sorption induced wall strain in vertical,

metal hydride based hydrogen storage container. J Alloy Compd. 2018;735:2675-84.
[21] Wang D, Wang Y, Huang Z, Yang F, Wu Z, Zheng L, et al. Design optimization and sensitivity analysis of the radiation mini-channel metal hydride reactor. Energy. 2019;173:443-56.
[22] Malleswararao K, Aswin N, Srinivasa Murthy S, Dutta P. Studies on a dynamically coupled multifunctional metal hydride thermal battery. J Alloy Compd. 2021;866:158979.
[23] Karmakar A, Mallik A, Gupta N, Sharma P. Studies on 10 kg alloy mass metal hydride based reactor for hydrogen storage. Int J Hydrog Energy. 2021;46:5495-506.
[24] Cao Y, Ke H, Klemeš JJ, Zeng M, Wang Q. Comparison of aerodynamic noise and heat transfer for shell-and-tube heat exchangers with continuous helical and segmental baffles. Appl Therm Eng. 2021;185:116341.
[25] Maakoul AE, Laknizi A, Saadeddine S, Metoui ME, Zaite A, Meziane M, et al. Numerical comparison of shell-side performance for shell and tube heat exchangers with trefoil-hole, helical and segmental baffles. Appl Therm Eng. 2016;109:175-85.
[26] Shah RK, Sekuli DP. Fundamentals of heat exchanger design, 2003, pp. 436-437.
[27] Wang X, Liang Y, Sun Y, Liu Z, Liu W. Experimental and numerical investigation on shell-side performance of a double shell-pass rod baffle heat exchanger. Int J Heat Mass Tran. 2019;132:631-42.
[28] Shih T-H, Liou WW, Shabbir A, Yang Z, Zhu J. A new k-ϵ eddy viscosity model for high reynolds number turbulent flows. Comput Fluids. 1995;24:227-38.
[29] Zhu Z, Zhu S, Zhao X, Cheng H, Yan K, Liu J. Effects of Ce/Y on the cycle stability and anti-plateau splitting of $La_{5-x}Ce_xNi_4Co$ (x=0.4, 0.5) and $La_{5-y}Y_yNi_4Co$ (y=0.1, 0.2) hydrogen storage alloys. Mater Chem Phys. 2019;236:121725.
[30] Dhaou H, Askri F, Salah MB, Jemni A, Ben Nasrallah S, Lamloumi J. Measurement and modelling of kinetics of hydrogen sorption by $LaNi_5$ and two related pseudobinary compounds. Int J Hydrogen Energy. 2007;32:576-87.
[31] Ma J, Wang Y, Shi S, Yang F, Bao Z, Zhang Z. Optimization of heat transfer device and analysis of heat & mass transfer on the finned multi-tubular metal hydride tank. Int J Hydrog Energy. 2014;39:13583-95.
[32] Dhaou H, Mellouli S, Askri F, Jemni A, Ben Nasrallah S. Experimental and numerical study of discharge process of metal–hydrogen tank. Int J Hydrogen Energy. 2007;32:1922-7.
[33] Hariyadi A, Suwarno S, Denys RV, von Colbe JB, Sætre TO, Yartys V. Modeling of the hydrogen sorption kinetics in an AB_2 laves type metal hydride alloy. J Alloy Compd. 2022;893:162135.
[34] Singh A, Maiya MP, Srinivasa Murthy S. Effects of heat exchanger design on the performance of a solid state hydrogen storage device. Int J Hydrog Energy. 2015;40:9733-46.
[35] Lototskyy MV, Tolj I, Davids MW, Klochko YV, Parsons A, Swanepoel D, et al. Metal hydride hydrogen storage and supply systems for electric forklift with low-temperature proton exchange membrane fuel cell power module. Int J Hydrog Energy. 2016;41:13831-42.
[36] Lototskyy MV, Davids MW, Tolj I, Klochko YV, Sekhar BS, Chidziva S, et al. Metal hydride systems for hydrogen storage and supply for stationary and automotive low temperature PEM fuel cell power modules. Int J Hydrog Energy. 2015;40:11491-7.